In the format provided by the authors and unedited.

Site-selective CO disproportionation mediated by localized surface plasmon resonance excited by electron beam

Wei-Chang D. Yang [1,2], **Canhui Wang** [1,2], **Lisa A. Fredin** [3], **Pin Ann Lin** [1,2], **Lisa Shimomoto** [1], **Henri J. Lezec** [1] **and Renu Sharma** [1]*

[1]Physical Measurement Laboratory, National Institute of Standards and Technology, Gaithersburg, MD, USA. [2]Maryland NanoCenter, University of Maryland, College Park, MD, USA. [3]Material Measurement Laboratory, National Institute of Standards and Technology, Gaithersburg, MD, USA.
*e-mail: renu.sharma@nist.gov

Supplementary Information

Site-selective CO disproportionation mediated by localized surface plasmon resonance excited by electron beam

Wei-Chang D. Yang[1,2], Canhui Wang[1,2], Lisa A. Fredin[3], Pin Ann Lin[1,2], Lisa Shimomoto[1], Henri J. Lezec[1] and Renu Sharma[1*]

1. Physical Measurement Laboratory, National Institute of Standards and Technology, Gaithersburg, Maryland 20899

2. Maryland NanoCenter, University of Maryland, College Park, Maryland 20742

3. Material Measurement Laboratory, National Institute of Standards and Technology, Gaithersburg, Maryland 20899

I. Density-functional theory (DFT) calculations for CO adsorption and disproportionation on Au surfaces.
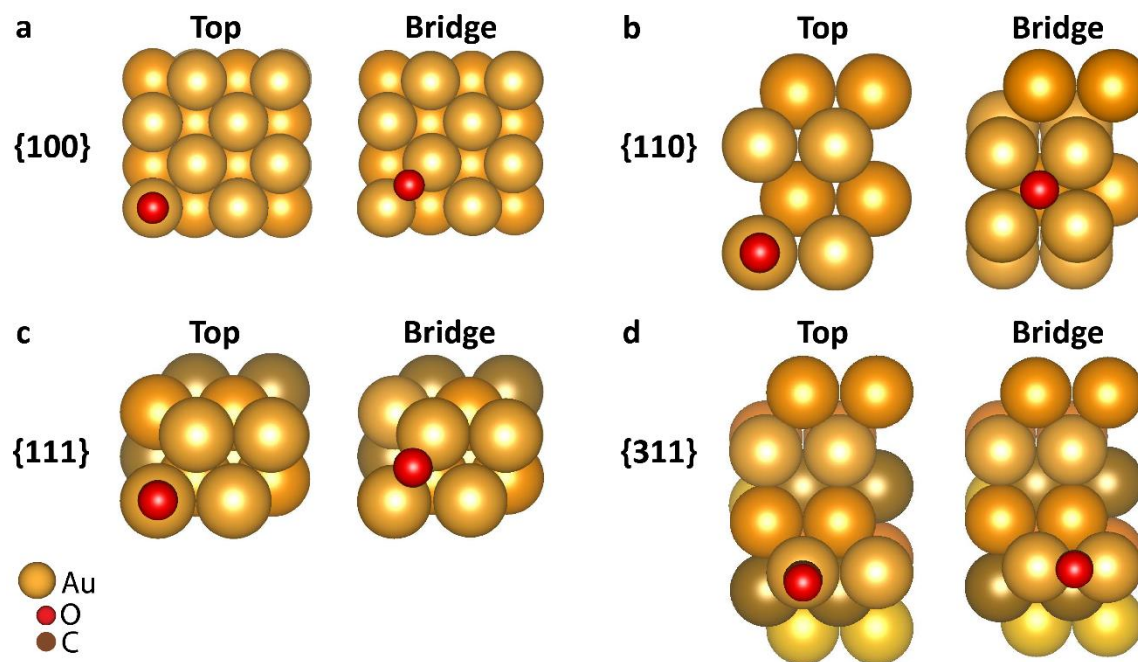
Supplementary Figure 1 | Configurations of CO adsorption sites on Au surfaces. Top-view of CO adsorption at the top and bridge sites on **a,** {100}, **b,** {110}, **c,** {111}, and **d,** {311} Au surfaces via the C atom (shadowed by the O atom in the view direction).

Supplementary Table 1 | Density-functional theory (DFT) calculations of CO adsorption energies on Au surfaces. Calculated adsorption energies ($E_{ads} = E_{Au} + E_{CO} - E_{Au-CO}$, eV) of CO on Au surfaces formed by various crystallographic planes. Literature data are referenced; otherwise, the values are obtained in this work. The optimized configurations of top, bridge, and hollow sites with respect to each Au surface are shown in Supplementary Fig. 1. PBE-GGA stands for Perdew-Burke-Ernzerhof generalized gradient approximation and PW91 represents the GGA proposed by Perdew and Wang (see Methods).

| Au surface	Site	E_{ads} (eV)	DFT
{1 0 0}	Top	-0.48	PBE
	Bridge	-0.62	PBE
{1 1 0}	Top	-0.63	PBE
	Bridge	-0.33	PBE
	Short bridge	-0.54	PW91[1]
{1 1 1}	Top	-0.18	PBE
	Bridge	-0.20	PBE
{2 1 1}	Bridge	-1.05	PBE[2]
	Bridge	-0.66	PW91[3]
{2 2 1}	Bridge	-1.00	PBE[2]
{2 -3 0}	Top	-0.73	PW91[4]
{3 2 1}	Top	-0.77	PW91[5]
{3 2 2}	Top	-0.63	PBE[6]
{3 1 1}	Top	-1.10	PBE
	Bridge	-1.11	PBE
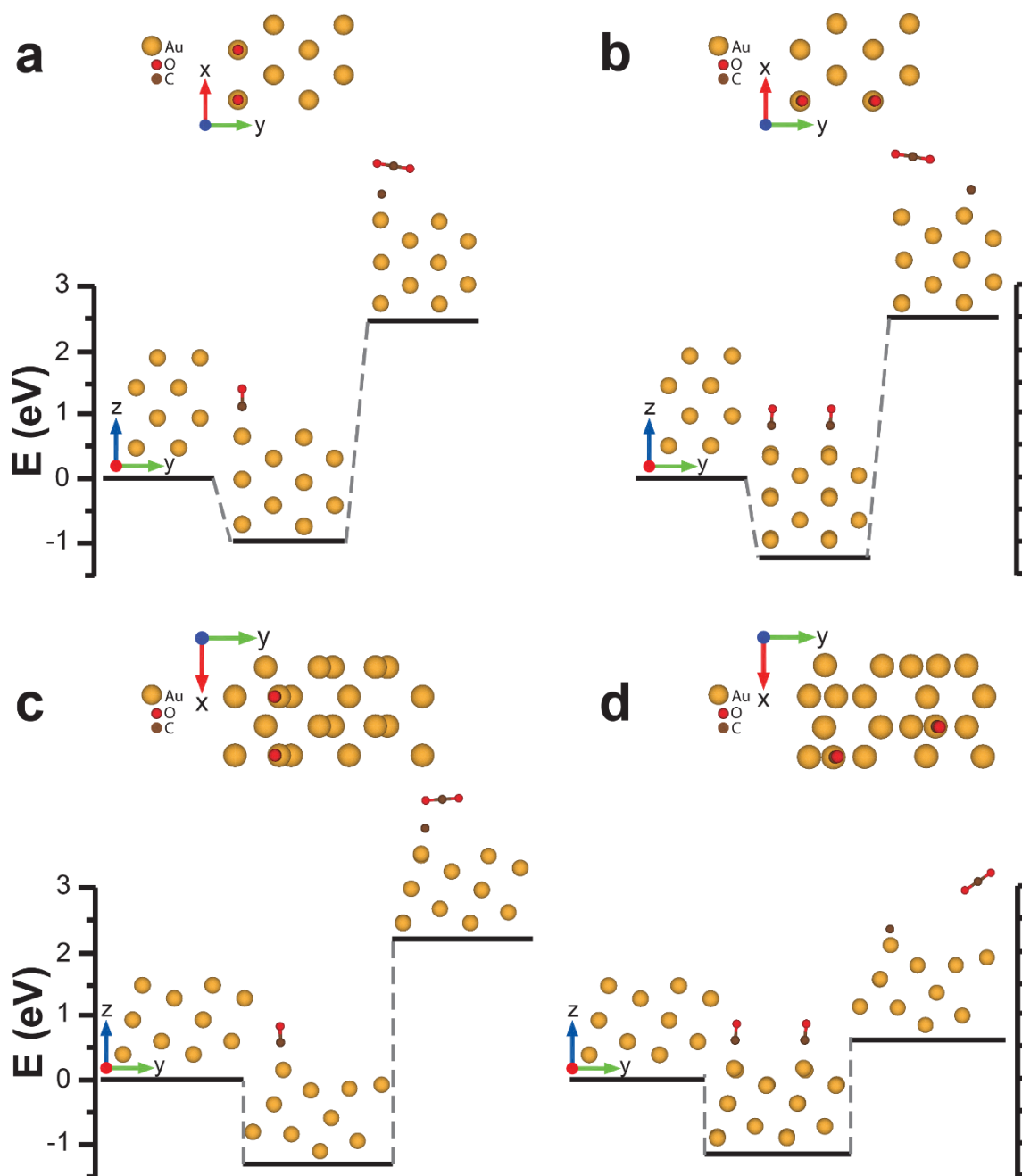
Supplementary Figure 2 | Calculated energy diagrams of CO disproportionation on Au surfaces. Changes in energy from (left to right in each panel) a clean surface of **a-b,** Au {110} and **c-d,** Au {311}, respectively, to adsorption of two CO molecules on each surface using two possible pairs of top sites that leads to different adsorption orientations (**a** versus **b** and **c** versus **d**, respectively), and finally, to C-deposited Au surfaces along with one free CO_2.

Supplementary Table 2 | List of calculated energies required for obtaining amorphous carbon on Au surfaces. Delta self-consistent field (SCF) energies ($E_{\Delta SCF} = E_{prod} - E_{react}$, eV) for the dissociation and disproportionation reaction on the Au {110} and {311} surfaces.

		{110}	{311}
dissociation	CO-Au → C-Au + O	11.11	11.16
disproportionation	CO-Au-CO → CO$_2$-Au-C	3.45	1.97

II.   Crystal structure measurement.

The crystal structure of the triangular Au nanoprisms is determined by measuring the electron diffraction patterns at a series of tilt angles. The STEM-ADF images (Supplementary Fig. 3 a-c) acquired at -30°, 0 °, and +30° tilts, respectively, show changes in the projected outlines of three Au nanoprisms anchored to TiO$_2$ support particles. The 3-dimensional (3D) image obtained by the tomographic reconstruction of a STEM-ADF image series shows the 3D location of each of the plate-like nanoprsims (Supplementary Fig. 3d). High-resolution TEM (HRTEM) image (Supplementary Fig. 3e) displays a Au nanoprism with a triangular outline with three rounded corners, while the corresponding electron diffractogram (inset of Supplementary Fig. 3e) indicates the nanoprism is aligned to the <111> zone axes of Au. The plate surface of the Au nanoprism is identified as the {111} plane using nanobeam diffraction (Supplementary Fig. 3f). When the plate surface is aligned to the <111> zone axes, the triangular outlines consist of three short edges and three long edges in the crystal model (Fig. 1b). The short edges are located at the junctions of {100} and {110} facets, whereas the long edges are the intersections of two {311} facets.
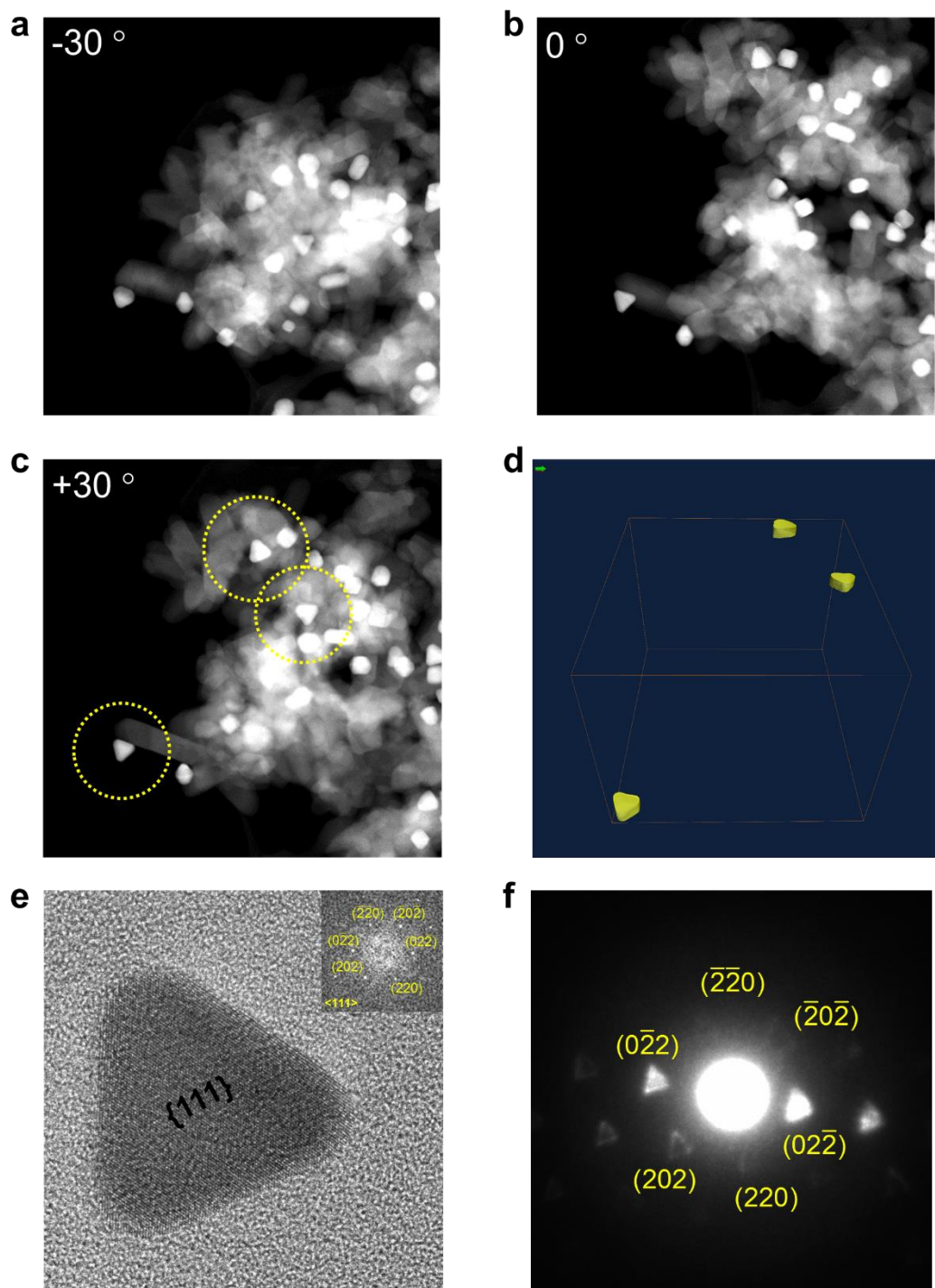
Supplementary Figure 3 | Crystal structure measurement of Au nanoprisms. STEM-ADF tilt series images of Au on TiO_2 at **a,** -30°, **b,** 0 °, and **c,** 30 °, **d,** 3D reconstruction. **e,** HRTEM image of Au nanoprism with a diffractogram to show the Au_{FCC} along the <111> zone axis (inset). The plate surface is identified as {111}. **f,** Nanobeam diffraction pattern, showing multiple dark field images, of the nanoprism along the <111> zone axis.
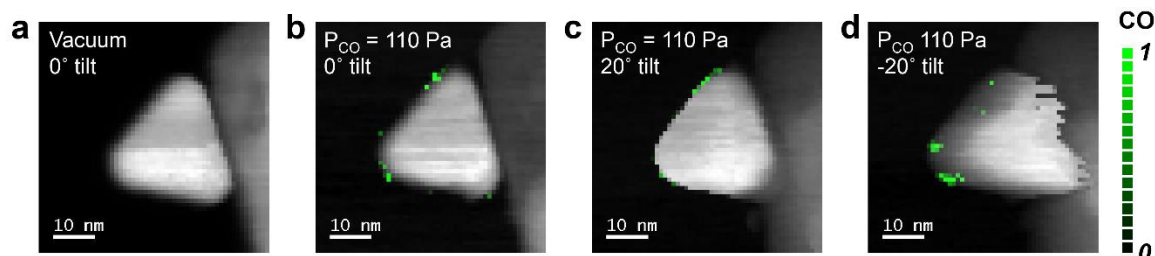
Supplementary Figure 4 | EELS Carbon K-edge maps to spatially resolve the adsorbed CO molecules on a Au nanoprism at various tilt angles. Spectrum images are acquired in both **a,** vacuum (V_i) and **b-d,** CO environment at P_{CO} = 110 Pa. **a,** C K-edge signal is not found on the surface of Au or TiO_2 in V_i. **b-d,** after removing the spectroscopic features from the environmental CO at individual pixels, the C K-edge maps at tilt angles of **b,** 0°, **c,** -20°, and **d,** 20° show the distribution of adsorbed CO at the edges of the Au nanoprism. The green contrast shows the normalized intensity of C K-edge signal integrated from 285 eV to 315 eV that originates from the adsorbed CO only. The visibility of the adsorbed CO at the edges is sensitive to the tilt angle from the <111> zone axis of Au which allows the edges to align in the line of sight of electron beam with no background signal from the Au nanoprism. This confirms that the adsorbed CO molecules are exclusively localized at the edges (junctions of {311}/{311} and {100}/{110) planes).

III. Numerical calculations of localized surface plasmon (LSP) resonance excited by electron beam.

Metallic nanoparticle boundary element method (MNPBEM) toolbox provides a boundary element method (BEM) approach that is designed to solve Maxwell's equations in a dielectric environment where matters with homogeneous and isotropic dielectric functions are divided by discretized interfaces consisting of vertices and faces of the boundary elements[7, 8].

The 3D structure of a triangular nanoprism was generated and meshed using Delaunay triangulation before loading into the MNPBEM toolbox, whereas the support particle was created by extruding a 2D polygon (a rectangle with rounded corners) along the Z direction, complying with a superellipse profile: $(x/a)^n + (y/b)^n = 1$, to form a cuboid in the toolbox. The combined 3D model (Supplementary Fig. 5a) creates discretized interfaces that separate vacuum

(environment), Au (nanoprism), and TiO_2 (cuboid). The nanoprism and cuboid have distinct dielectric functions that are derived from optical constants – refractive index (n) and extinction coefficient (k) – for Au and TiO_2, respectively, in the energy-loss range between 0.01 eV and 6 eV as reported in the literature[9, 10]. We use the retarded EELS simulations that justify electron trajectories, induced currents, and charges inside and outside the boundaries to obtain the surface charge induced by electron beam at the discretized surface (Supplementary Fig. 5). The simulated surface charges can be used to calculate the electron energy-loss probability with respect to electron beam (excitation) locations (Fig. 2a) and the results agree with the EELS data measured from Au nanoprsims supported by TiO_2 particles (Fig. 3a) of a similar configuration and dimensions to the 3D model. Distinct loss probability spectra at P1, P2, and P3 indicate that loss probability is related to the excitation-location-dependent coupling efficiency associated with the LSP mode on the Au surface. The integrated loss probability maps between 1.8 eV and 3.8 eV (Fig. 2b) show that the maximum loss probability occurs at the cantilevered nanoprism corner, suggesting it is the most efficient location to excite LSP modes.
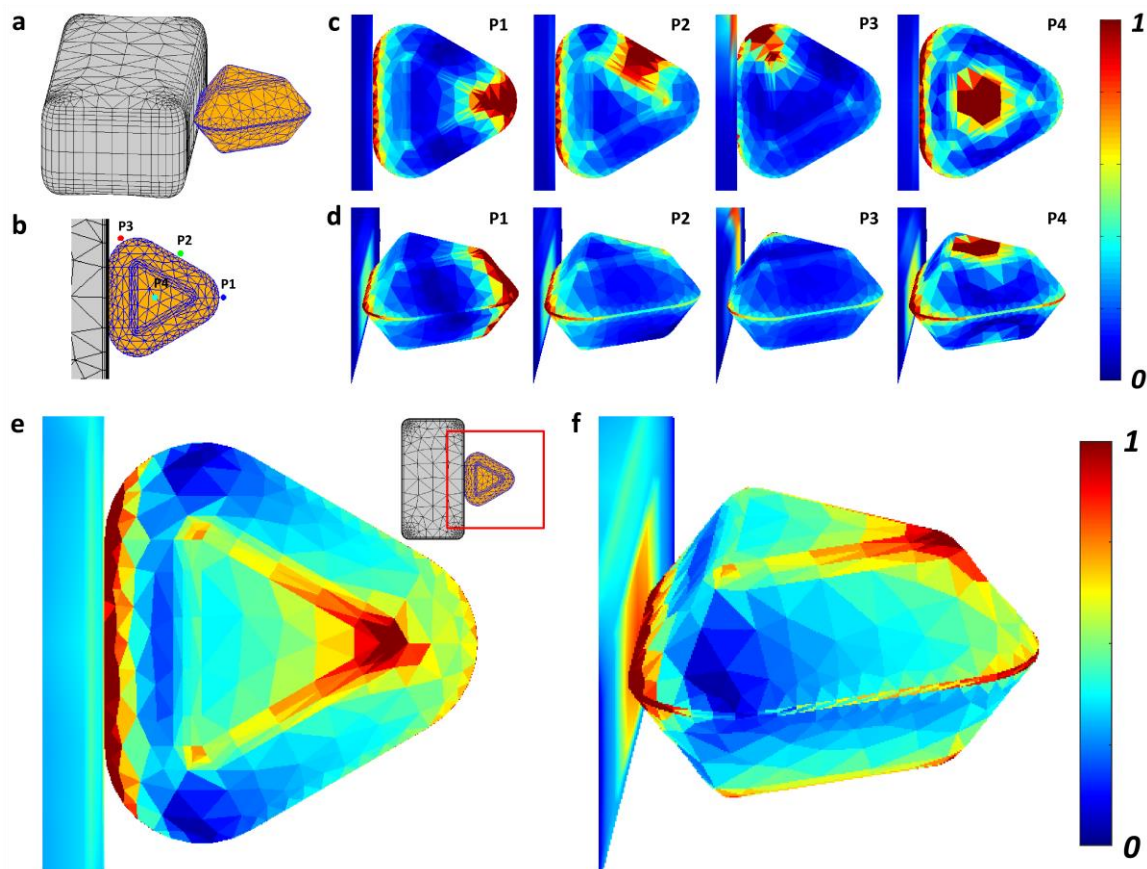
Supplementary Figure 5 | Numerical calculations of electron energy-loss probability derived from surface charge distributions induced by electron beam excitation of LSP resonances on a Au nanoprism supported on TiO₂. a, Discretized interfaces that separate the Au nanoprism (golden yellow) and the TiO_2 support (grey) from vacuum. **b,** Impact parameters indicating electron beam locations of P1, P2, P3 and P4 for the surface charge phasor calculations. **c-d,** Surface charge distributions induced by an 80 kV electron beam positioned at P1, P2, P3, and P4, respectively, illustrated using the normalized amplitudes of surface charge phasors integrated over 1.8 eV to 3.8 eV, from the top view (**c**), and the side view (**d**) with a 20° vertical elevation of the viewing angle. The color bar shows the normalized number of surface charges from 0 to the maximum on the Au surface in (**c**) and (**d**). **e-f,** Surface charge distribution induced by the raster scan of electron beam across a 50 nm by 50 nm area with a 1 nm spacing between each beam location (total 2,500 beam locations), illustrated using the normalized amplitudes of surface charge phasors integrated from 1.8 eV to 3.8 eV, viewed from the top (**e**), and the side (**f**) with a 20° vertical elevation of the viewing angle. The color bar shows the normalized number of surface charges from 0 to the maximum on the Au surface in (**e**) and (**f**).

Furthermore, we calculated the induced surface charges on the 3D structure (Supplementary Fig. 5a) in the energy-loss range between 1.8 eV and 3.8 eV – spanning the resonance peaks in

Fig. 2a – with respect to the electron-beam excitation locations of P1 to P4 (Supplementary Fig. 5b). The amplitude of surface charges in the phasor form ($e^{-i\omega t}$) at individual faces (Supplementary Fig. 5 c and d) indicates the normalized number of surface charges mediated by the respective beam position at $t = 0$, where t denotes time. The distributions of the surface charges with respect to P1, P2, P3, and P4 show a consistent spatial distribution that resembles a dipolar mode, well known as the fundamental mode of a flat triangular metallic nanoparticle[11]. The observed LSP energy blue-shift when electron beam is positioned at P2 (Fig. 2a) can be attributed to an increased contribution from the hexapole mode[12]. The likelihood of exciting such modes within the electron energy-loss range between 1.8 eV and 3.8 eV on a Au nanoprism of similar dimensions on TiO$_2$ is further supported by simulating the surface charge distribution that results from the raster scans of electron beam across the entire nanoprism. We calculated the induced surface charge phasors using each of the 2,500 beam locations with a 1 nm spacing between each other that form an array extending a 50 nm by 50 nm area (inset of Supplementary Fig. 5e). The surface charge distribution, which is derived from the amplitude of the surface charge phasors integrated over 1.8 eV to 3.8 eV at individual faces, confirms the segregation of surface charges at the cantilevered corner (Supplementary Fig. 5 e and f).

Next, to understand the relationship between the loss probability and electric field, we simulated the electric field amplitude distribution for the same Au nanoprism on TiO$_2$ support using MNPBEM. The spatial distributions of electric field amplitude generated by the excitation from an electron beam placed at various locations: three aloof positions at P1, P2, and P3 as well as one direct impact position at P4 for Au/TiO$_2$, are shown in Supplementary Fig. 6 a-d. Although the electric field amplitude is enhanced in the vicinity of each electron beam location at P1, P2 and P3, electric field amplitudes are present at all the three nanoprism corners (Supplementary Fig. 6

a-d) as well, suggesting that the local field enhancement originates from the electron-beam-excited LSP resonance on the Au nanoprism. The similar local field enhancement also takes place, when electron beam directly impacts the Au nanoprism at P4.
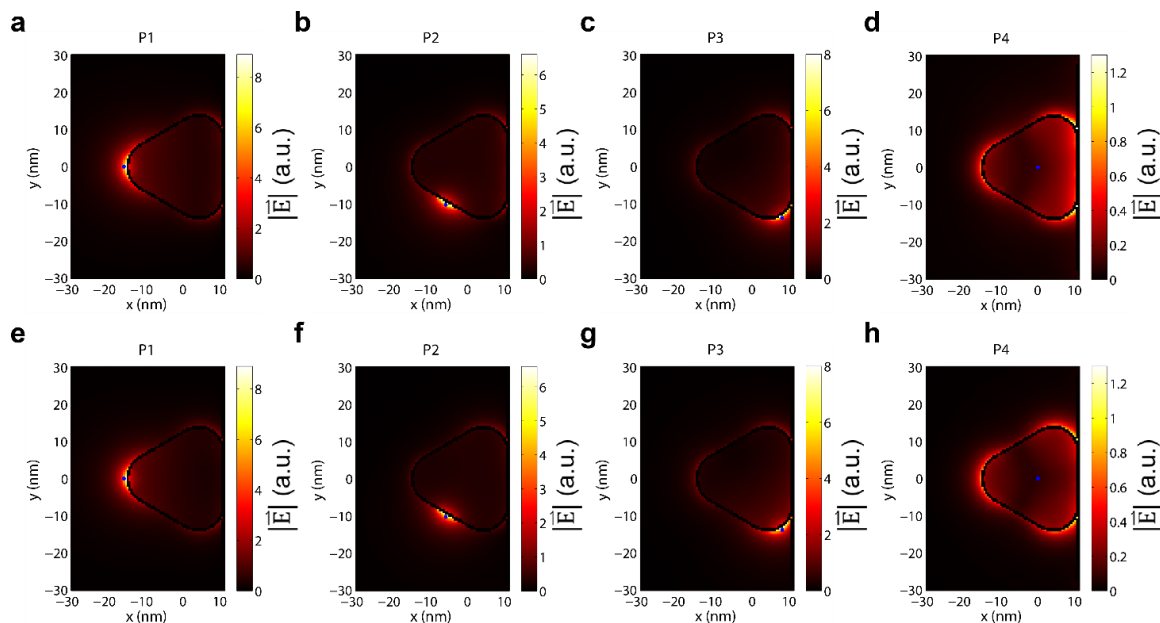

Supplementary Figure 6 | Simulated induced electric field maps using MNPBEM. Induced electric field of the LSP resonance on a Au nanoprism on either TiO_2 (**a - d**) or SiO_2 (**e - h**) support excited by electron beam (80 kV) at three aloof positions outside the Au nanoprism: P1 (**a, e**), P2 (**b, f**), and P3 (**c, g**), and one direct-impact position at the body center of the projected Au nanoprism: P4 (**d, h**), with respect to the resonance energies at these beam positions. Electron beam position in each panel is indicated by a blue point.

The probability of exciting LSP resonance is known to be relevant to the photonic local density of states (LDOS). However, the spatial distribution of simulated LDOS, excited by placing a dipole (along the electron beam trajectory, z) at the center plane (perpendicular to the electron beam trajectory at z = 0) of a flat, symmetric nanostructure, has been reported to have no direct quantitative connection to loss probability maps due to the difference between coupling of electron beam or a dipole to LSP resonance on a flat metallic plate using the boundary element method[13].

On the other hand, we found that the simulated LDOS spectra (Supplementary Fig. 7a) using MNPBEM, when the dipole excitation is placed at z = 8 nm which is leveled with the top plate surface of the Au nanoprism on TiO_2 support (Supplementary Fig. 7b), show qualitative correlation to the simulated electron energy-loss probability (Supplementary Fig. 7a), in agreement with simulated results reported by Losquin *et al.*[12], and the experimental low-loss EELS (Fig. 3b). LDOS excited by the dipole excitation at the projected positions of P1, P2, and P3 shows peak centers at 2.3420 eV ± 0.0006 eV, 2.4372 eV ± 0.0005 eV, and 2.2814 eV ± 0.0010 eV, respectively. The maximum LDOS (blue solid line, Supplementary Fig. 7a) at the dipole position of projected P1 (turquoise marker, Supplementary Fig. 7b) shows the direct link to the maximum loss probability (blue dash line, Supplementary Fig. 7a) at the electron beam position of P1 due to the excitation of LSP resonance on the Au nanoprism. It is important to note that the result is the same when the dipole excitation is placed at z = - 8 nm which is leveled with the bottom plate surface of the Au nanoprism. LDOS excited at various z with respect to the center plane (z = 0 nm) of the Au nanoprism show changes in peak energy, line width and shape (Supplementary Fig. 7c). This may be caused by the fact that a dipole has a lateral distance (d) dependence of $1/d^2$, which makes the LDOS excitation extremely sensitive to the boundary surface on the edges of the Au nanoprism. Therefore, positioning the dipole excitation leveled with one of the two plate surfaces results in the LDOS that can be related to the electron energy-loss probability using near-field (aloof) electron beam excitation that minimizes the influence of the boundary surface at the nanoprism edges. Furthermore, the simulated LDOS maps (Supplementary Fig. 8 a-c) using the resonance energies associated with the three dipole positions (2.342 eV, 2.4372 eV, and 2.2814 eV), respectively, show reasonable agreements with the simulated loss probability maps (Supplementary Fig. 9 a-c) for the resonance energies at the three electron beam positions of P1,

P2, and P3 (2.337 eV, 2.387 eV, and 2.283 eV), respectively. This qualitatively shows that the coupling between the near-field excitation and the LSP resonance on a Au nanoprism on TiO_2 support create the excess LDOS at the cantilevered nanoprism corner (Supplementary Fig. 8 a-c), leading to enhanced loss probability at this specific corner (Supplementary Fig. 9 a-c).
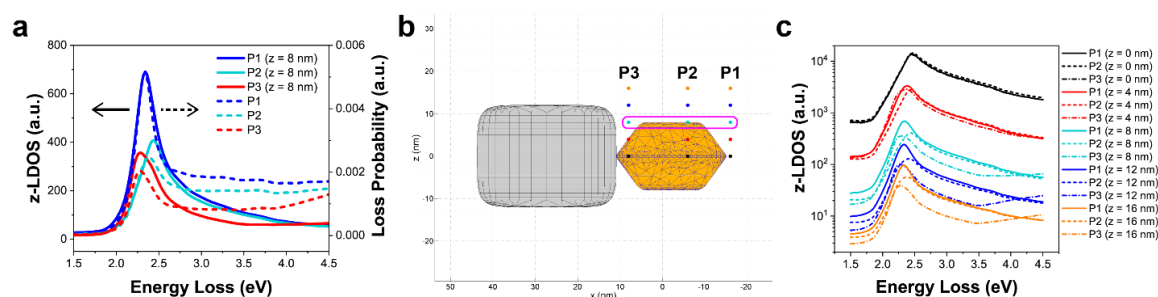
Supplementary Figure 7 | Simulated photonic local density of states using MNPBEM. a, photonic local density of states (LDOS) excited by placing a dipole along the z direction at z = 8 nm (solid lines), which is in level with the top plate surface of a Au nanoprism on TiO_2 support, indicated by the turquoise markers in **b**, in comparison with loss probability simulated by placing electron beam at P1, P2, and P3 (dash line; also shown in Fig. 2a). **b,** Various dipole positions along the z direction of the projected P1, P2, and P3 positions used for the simulated LDOS spectra in **c**. **c,** LDOS excited by placing a dipole at various z with respect to the center plane of the Au nanoprism (z = 0 nm).
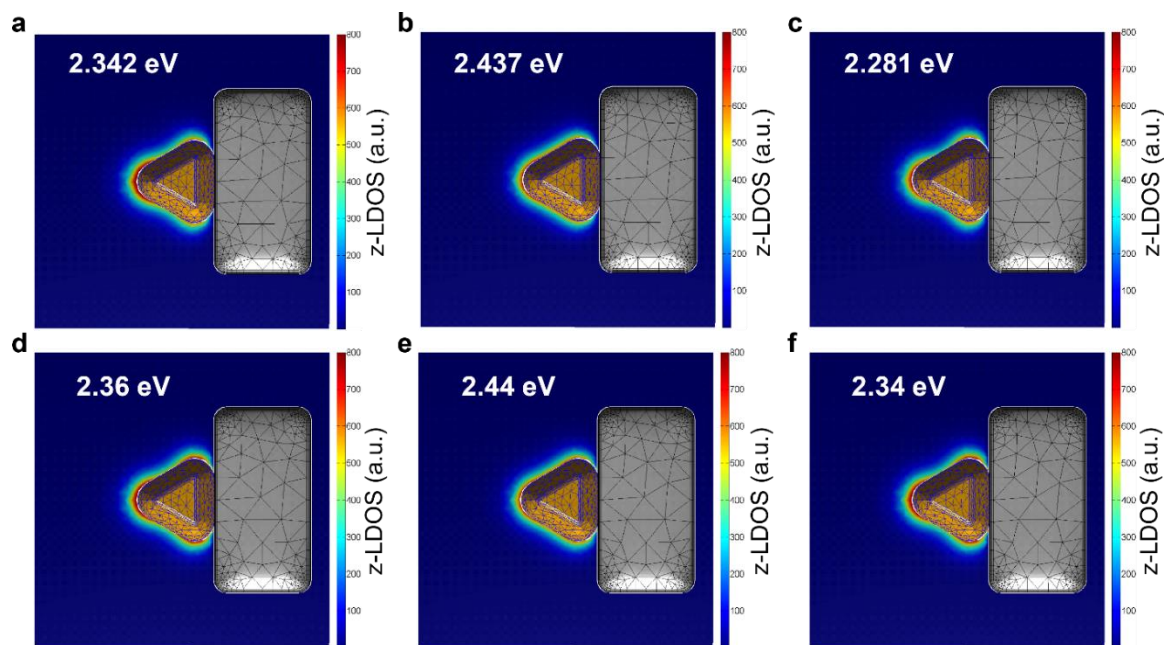
Supplementary Figure 8 | Simulated photonic local density of states maps using MNPBEM. Spatial distributions of LDOS excited by placing a dipole along the z direction at z = 8 nm, which is at the same level as the top plate surface of a Au nanoprism on TiO_2 support (**a - c**) or SiO_2 (**d - f**), with respect to the resonance energies associated with the three dipole positions circled (magenta) in Supplementary Fig. 7b.
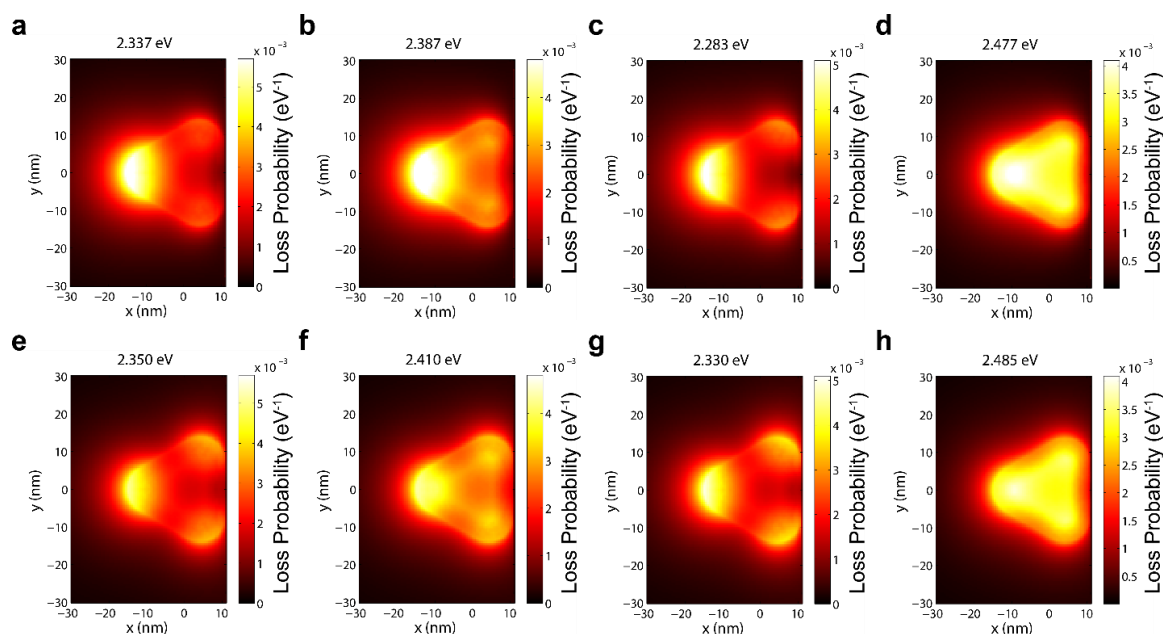
Supplementary Figure 9 | Simulated loss probability maps using MNPBEM. Loss probability maps using electron beam (80 kV) interacting with a Au nanoprism on either TiO_2 (**a - d**) or SiO_2 (**e - h**) support. Electron beam is placed at three aloof positions outside the Au nanoprism: P1 (**a, e**), P2 (**b, f**), and P3 (**c, g**), and one direct-impact position at the body center of the projected Au nanoprism: P4 (**d, h**), with respect to the resonance energies associated with those beam positions, denoted in Supplementary Fig. 6.

The simulations were also performed using SiO_2 as the support material, as shown in Supplementary Fig. 6 e-h, Fig. 8 d-f, Fig. 9 e-h, and Fig. 10b. Based on our simulation results, the maximum loss probability in each map (Supplementary Fig. 10) for the specific resonance energy at P1, P2, P3, and P4 drops about 18 %, 25 %, 8 %, and 9 %, respectively, when changing the support material from TiO_2 to SiO_2, suggests a decreased probability to excite the LSP resonance mode at these electron beam positions. The photonic LDOS maps for the resonance energies at the three dipole positions (Supplementary Fig. 8 d-f) indicate the decrease in LDOS when placing the dipole outside the cantilevered nanoprism corner for SiO_2 support. On the other hand, the maximum electric field amplitude (Supplementary Fig. 6) for each of the electron beam positions

at P1, P2, and P4 decreases by about 3 %, 5 %, and 24 %, respectively, but increases about 13 %

at P3, when the support material is changed from TiO_2 to SiO_2.
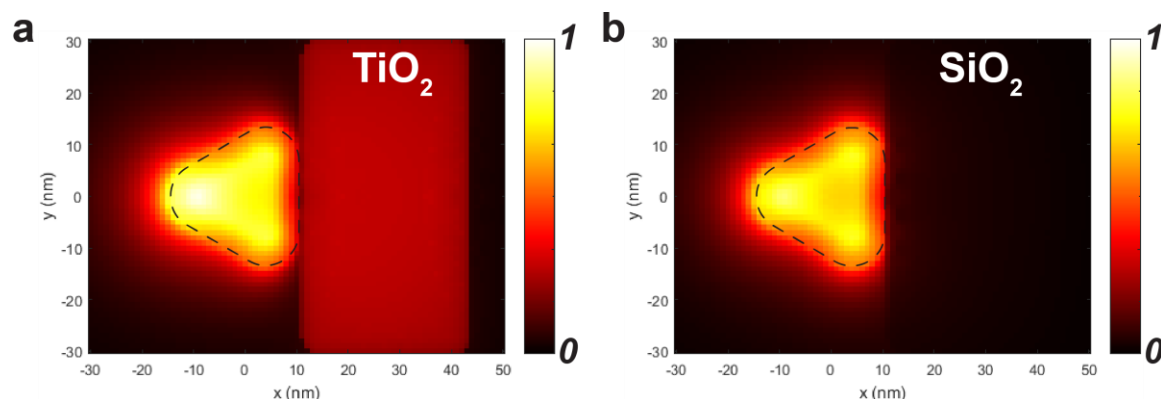

Supplementary Figure 10 | Simulations of loss probability maps due to electron-beam-excited LSP modes on Au nanoprism supported by various support materials. SiO_2 is selected as an alternate to TiO_2 and its optical constant table[14] is loaded for the dielectric functions of the support particle. The loss probability map integrated over 1.8 eV to 3.8 eV shows its reduced probability to excite the LSP modes by the electron beam positions at the cantilevered corner compared to the use of TiO_2. **a,** TiO_2 support shows increased loss probabilities at the cantilevered corner on and outside the Au nanoprism. **b,** SiO_2 support leads to attenuated loss probabilities at the cantilevered nanoprism corner, which is less distinct in loss probability from the other two corners anchored to the SiO_2 support. Note that both maps use the same intensity scale which is normalized to the maximum intensity in b. The dashed outline indicates the edges of the Au nanoprism.

IV. EELS data
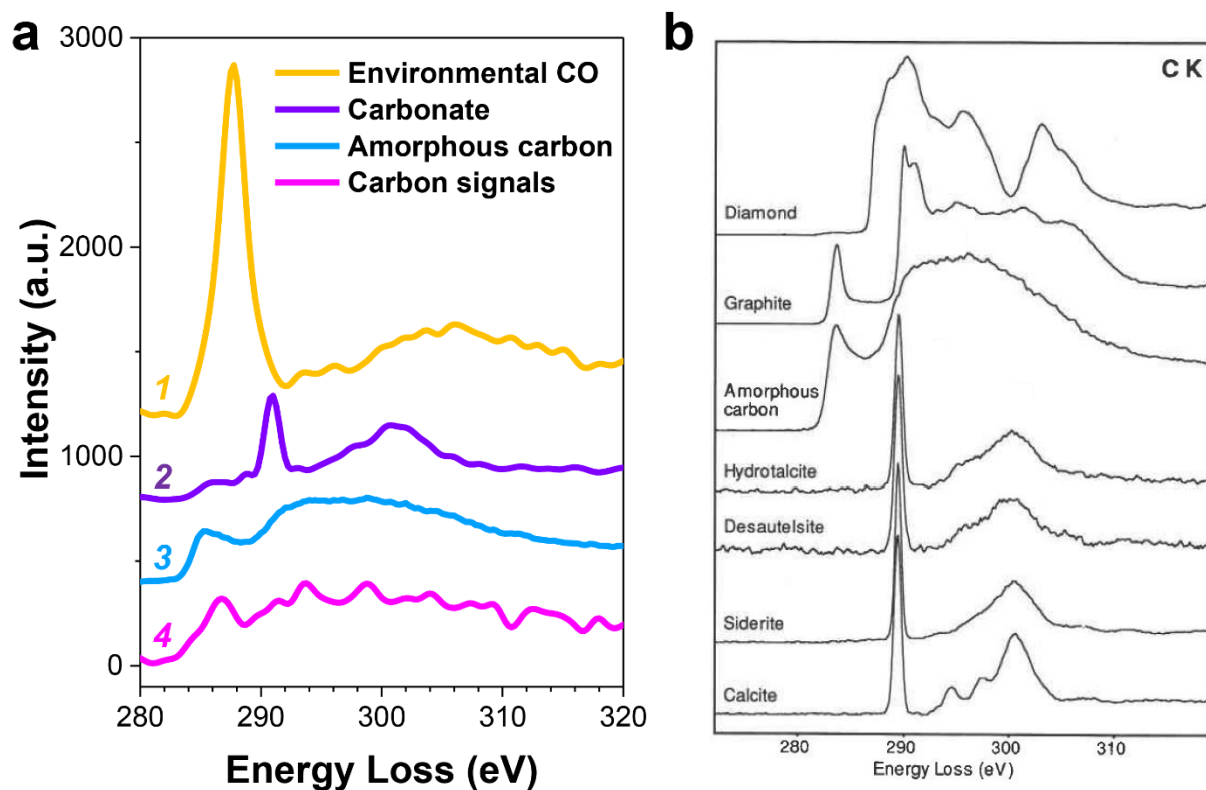
Supplementary Figure 11 | EELS data displaying distinct carbon K-edges of chemical substances containing carbon. a, Carbon K-edges of (1) CO, (2) sodium carbonate, (3) amorphous carbon film coated on lacey/formvar grids, and (4) amorphous carbon deposited on Au nanoprisms in a CO disproportionation reaction driven by electron beam excited LSP resonance, which are all measured in the ESTEM. Spectra are arbitrarily shifted in y-axis for clarity. Also, CO peak has low signal to background ratio as it is from the gaseous region of the sample instead of solid areas, i.e. low t/λ. **b,** EELS data showing carbon K-edges of diamond, graphite, amorphous carbon and various carbonates (hydrotalcite, desautelsite, siderite, and calcite). Panel **b** adapted with permission from ref. [15], Mineralogical Society of America.
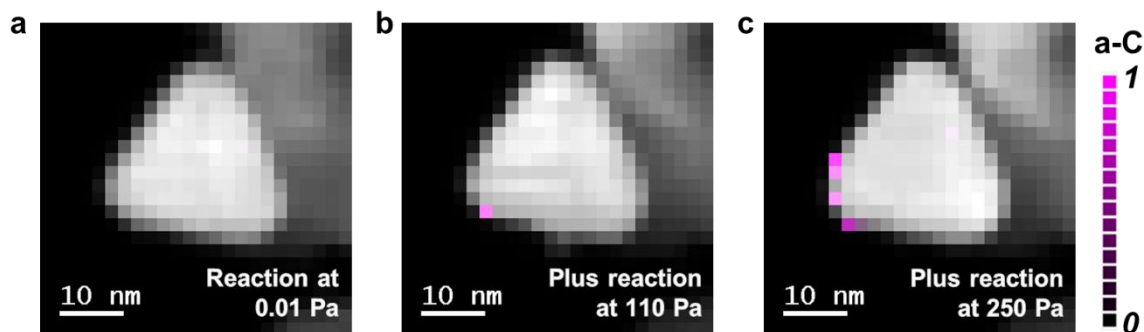
Supplementary Figure 12 | STEM-EELS maps of carbon K-edge collected after CO exposure (V_f) during the cycling of raster scans of electron beam on Au/TiO₂ in CO environment and after the evacuation of CO. In **a**, the absence of carbon K-edge signal indicates CO disproportionation does not take place or the amount of produced amorphous carbon (a-C) is lower than the detection limit of EELS during the raster scans at $P_{CO} = 0.01$ Pa. In **b**, after another cycle of raster scans at $P_{CO} = 110$ Pa, amorphous carbon (magenta) builds up near the cantilevered particle corner. In **c**, following the third cycle of raster scans at $P_{CO} = 250$ Pa, amorphous carbon deposits cover most of the cantilevered corner. The location of carbon deposits confirms CO disproportionation due to the superimposed location of the CO adsorption sites and the maximum intensity of electron-beam-excited LSP resonance.

V. References

1. Hussain A, Curulla Ferré D, Gracia J, Nieuwenhuys BE, Niemantsverdriet JW. DFT study of CO and NO adsorption on low index and stepped surfaces of gold. *Surface Science* 2009, **603**(17)**:** 2734-2741.

2. Liu Z-P, Hu P, Alavi A. Catalytic role of gold in gold-based catalysts: A density functional theory study on the CO oxidation on gold. *Journal of the American Chemical Society* 2002, **124**(49)**:** 14770-14779.

3. Mavrikakis M, Stoltze P, Norskov JK. Making gold less noble. *Catal Lett* 2000, **64**(2-4)**:** 101-106.

4. Loffreda D, Sautet P. First-principles study of CO adsorption and vibration on Au surfaces. *J Phys Chem B* 2005, **109**(19)**:** 9596-9603.

5. Fajin JLC, Cordeiro MNDS, Gomes JRB. DFT Study of the CO Oxidation on the Au(321) Surface. *J Phys Chem C* 2008, **112**(44)**:** 17291-17302.

6. Yim WL, Nowitzki T, Necke M, Schnars H, Nickut P, Biener J, *et al.* Universal phenomena of CO adsorption on gold surfaces with low-coordinated sites. *J Phys Chem C* 2007, **111**(1)**:** 445-451.

7. Hohenester U, Trügler A. MNPBEM – A Matlab toolbox for the simulation of plasmonic nanoparticles. *Computer Physics Communications* 2012, **183**(2)**:** 370-381.

8. Hohenester U. Simulating electron energy loss spectroscopy with the MNPBEM toolbox. *Computer Physics Communications* 2014, **185**(3)**:** 1177-1187.

9. Johnson PB, Christy RW. Optical Constants of the Noble Metals. *Physical Review B* 1972, **6**(12)**:** 4370-4379.

10. Siefke T, Kroker S, Pfeiffer K, Puffky O, Dietrich K, Franta D, *et al.* Materials Pushing the Application Limits of Wire Grid Polarizers further into the Deep Ultraviolet Spectral Range. *Advanced Optical Materials* 2016, **4**(11)**:** 1780-1786.

11. Schmidt FP, Ditlbacher H, Hofer F, Krenn JR, Hohenester U. Morphing a plasmonic nanodisk into a nanotriangle. *Nano Lett* 2014, **14**(8)**:** 4810-4815.

12. Losquin A, Kociak M. Link between Cathodoluminescence and Electron Energy Loss Spectroscopy and the Radiative and Full Electromagnetic Local Density of States. *ACS Photonics* 2015, **2**(11)**:** 1619-1627.

13. Hohenester U, Ditlbacher H, Krenn JR. Electron-energy-loss spectra of plasmonic nanoparticles. *Phys Rev Lett* 2009, **103**(10)**:** 106801.

14. Gao L, Lemarchand F, Lequime M. Exploitation of multiple incidences spectrometric measurements for thin film reverse engineering. *Opt Express* 2012, **20**(14)**:** 15734-15751.

15. Garvie LAJ, Craven AJ, Brydson R. Use of Electron-Energy-Loss near-Edge Fine-Structure in the Study of Minerals. *Am Mineral* 1994, **79**(5-6)**:** 411-425.